Math. Model. Nat. Phenom. 19 (2024) 23
https://doi.org/10.1051/mmnp/2024019

Mathematical Modelling of Natural Phenomena
www.mmnp-journal.org

A HYDRODYNAMIC MODEL FOR THE HYDRAULIC JUMP AND INTERNAL WAVE GENERATION OVER A BOTTOM TOPOGRAPHY, THE CASE OF THE SAN ESTEBAN SILL IN THE GULF OF CALIFORNIA

Danalie de los Angeles Azofeifa-Chaves[1], Federico Angel Velázquez Muñoz[2], Anatoliy Filonov[2] and Miguel Angel Moreles[1,*]

Abstract. We are concerned with the mathematical and numerical modeling of hydrodynamic processes in the Gulf of California. The dynamic is driven by a forcing tide producing an inflow and outflow from the mouth of the Gulf to the northernmost part. When the tidal flow passes through the area of the Islands in the central part of the Gulf, it channels, increasing its speed. On the San Esteban Sill, a hydraulic jump is formed, then internal waves and solitons are released. Based on observational field campaigns, and hydrostatic 3D modeling, it is claimed that this is a cause–effect phenomenon. Hydrostatic models are unable to produce the groups of soliton-like waves. Consequently, we develop a non-hydrostatic version, a 2D vertical-slice model with the inclusion of density effects. Its hydrographic characteristics, such as stratification and bathymetric features, are modeled with appropriate initial and boundary conditions. The numerical solution is by a pressure projection method. The method is tested on benchmark problems and then applied to the Gulf of California. The data of the observational field campaigns are satisfactorily reproduced by the numerical results.

Mathematics Subject Classification. 35Q35, 76-10, 65Z05.

Received October 24, 2023. Accepted November 8, 2024.

1. Introduction

Ocean internal waves play an important role in the ocean's ecology, and research on the process of generation is of great relevance. Internal waves may form by tidal flow over topography generating mixing with some biological impacts, see the review in [1].

There is also an interest in understanding internal waves in the coastal areas as a source of alternative energy. In [2] a theoretical study is carried out in the case of vertical mixing. Therein, the topography is a continental slope gradually decreasing to the ocean bottom. The forcing tidal current is modeled as a basic time dependent

Keywords and phrases: Vertical-slice non-hydrostatic model, hydraulic jump, internal wave.

[1] Mathematics Department, Centro de Investigación en Matemáticas, Jalisco S/N, Valenciana,Guanajuato GTO 36023, Mexico.
[2] Physics Department, Universidad de Guadalajara, Blvd. Marcelino García Barragán 1421, Guadalajara JAL 44430, Mexico.

* Corresponding author: moreles@cimat.mx

harmonic flow. The point of the study is the efficiency of vertical mixing in the deep ocean by means of spectral analysis in a linear approximation.

In this work, we delve into the process of internal wave generation in a nonlinear hydrodynamic model including hydrographic characteristics, such as stratification and bathymetric features. This research is motivated by the hydrodynamic processes in the Gulf of California (GC). The dynamic is driven by a forcing tide producing an inflow and outflow from the mouth of the Gulf to the northernmost part, [3]. When the tidal flow passes through the area of the Islands in the central part of the Gulf, it channels, increasing its speed. Between the Islands, there are seamounts where the hydraulic jump is formed and packages of internal waves and solitons are released.

There are numerous studies that show evidence of the passage of internal waves in different places of the GC, such as the San Esteban Sill, and the Ballenas Channel, for instance, [4], [5].

In most of these studies, satellite images are used to identify the internal waves when they are already formed, without knowing exactly what the generation mechanism and the processes inside the ocean are. In other studies, they use sampling systems with anchors, limiting the measurements to specific sites without being able to precisely evaluate the spatial variations of the internal waves.

Some of the most intensive observational field campaigns in the area were carried out in 2007 and depth sections of temperature and salinity were obtained passing over the San Esteban Sill, [5]).

The results of these samplings led them to propose the hypothesis that the generation of internal tidal waves follows the formation of a hydraulic jump in the San Esteban Sill that travels to the north of the Gulf.

Using the 3D POM (Princeton Ocean Model), [6], some efforts to model the internal wave generation process are shown, which explains the main characteristics of the waves. It is argued, that it gives a fair reproduction of the vertical density fronts arising at the moment of creating a hydraulic jump. However the model is hydrostatic, consequently, it is unable to produce the groups of soliton-like waves found in their measurements.

To overcome these shortcomings, in this work, we develop a numerical non-hydrostatic 2D vertical slice model. We obtain more realistic dynamics of the internal tide when it passes over the San Esteban Sill. The model yields in tandem the hydraulic jump and the generation of internal wave packets and solitons. Moreover, the data of the aforementioned observational field campaigns are satisfactorily reproduced by the numerical results.

To our knowledge, non-hydrostatic 2D vertical slice models for internal wave generation applied to field cases are scarce at best. Most works are tested on synthetic benchmark cases, see for instance [7]. Therein, small-size lab experiments are studied, as well as an idealized Gaussian-shaped ridge.

The outline of this manuscript is as follows. In Section 2, we introduce the vertical slice ocean model for density-driven flows. Then a Pressure Projection method is developed for the solution. The numerical model is tested with a benchmark example, namely, a density-driven flow in a closed channel with variable impervious bathymetry. The data-driven application to the San Esteban Sill in the Gulf of California is presented in Section 3. The formation of the hydraulic jump and the generation of internal tidal waves are illustrated. Future work and conclusions are the content of Section 4.

2. Density-driven flow with variable bottom topography

Let us consider density-driven flows in the ocean modeled as a vertical slice. The compressible Newtonian flow Navier–Stokes equations are simplified as follows, see [8].

Flow and gradients of variables normal to the vertical slice are assumed to vanish, and the Coriolis force is ignored. Modeling is considered in the Cartesian coordinate system, in which x, y denote the horizontal coordinates, and the slice is along the $x-$axis. Changes are constant on $y-$cross sections, all the normal forces to this slice are neglected. The vertical axis z points upward to the undisturbed surface water located at $z = 0$, η is the free surface water, h_0 is the undisturbed water depth, and h is the total depth.

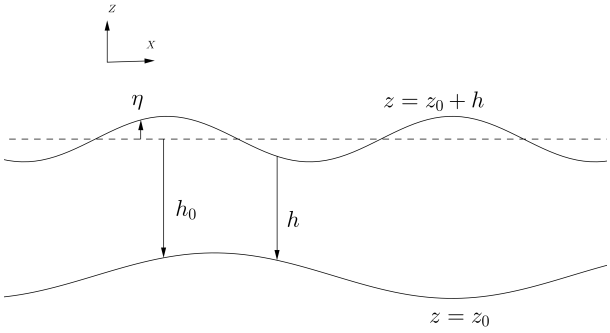

Figure 2. Topography of the slice x, z.

Let u, w be the velocities in direction x, z respectively, A_h, A_z the horizontal and vertical Eddy viscosities parameters, ρ the water's density, ρ_0 water's mean density, and P the dynamic pressure.

Density variations are small in the oceanographic problem under study, and the Boussinesq approximation is appropriate. It states that the density variation is only important in the buoyancy term $(\rho - \rho_0)g$ and can be neglected in the rest of the continuity and momentum equations, where ρ is set to ρ_0.

Under the Boussinesq approximation, the continuity equation reduces to the incompressible form

$$\nabla \cdot (u, w) = 0,$$

whereas the momentum equations become

$$\begin{aligned} \tfrac{\partial u}{\partial t} &= -\tfrac{1}{\rho_0}\tfrac{\partial P}{\partial x} - (u,w)\cdot\nabla u + \nabla\cdot\left(\begin{pmatrix} A_h & 0 \\ 0 & Az \end{pmatrix}\nabla u\right), \\ \tfrac{\partial w}{\partial t} &= -\tfrac{1}{\rho_0}\tfrac{\partial P}{\partial z} - (u,w)\cdot\nabla w + \nabla\cdot\left(\begin{pmatrix} A_h & 0 \\ 0 & A_z \end{pmatrix}\nabla w\right) - \tfrac{\rho-\rho_0}{\rho_0}g, \end{aligned}$$

Let us split $P = p + q$ in terms of hydrostatic and non-hydrostatic pressure. The former is with reference to an undisturbed sea level and is given by

$$\frac{\partial p}{\partial z} = -(\rho - \rho_0)g$$

with $p = 0$ at the sea surface.

The evolution of the sea level is described by the volume-conservation equation,

$$\frac{\partial \eta}{\partial t} = -\frac{\partial}{\partial x}(h < u >), \quad < u >= \frac{1}{h}\int_{-h_0}^{\eta} u \mathrm{d}z.$$

This equation is coupled to the momentum equations relating η and P at the undisturbed sea surface ($z = 0$). Applying the hydrostatic approximation

$$P_s = \rho_0 g \eta.$$

By the splitting of P_s we have $q_s = \rho_0 g \eta$, and we are led to

$$\frac{\partial q_s}{\partial t} = -\rho_0 g \frac{\partial}{\partial x}\int_{-h_0}^{\eta} u \mathrm{d}z.$$

Density effects are included in the vertical ocean-slice model by adding an advection–diffusion equation for density, namely

$$\frac{\partial \rho}{\partial t} = -(u,w)\cdot\nabla\rho + \nabla\cdot\left(\begin{pmatrix} K_h & 0 \\ 0 & K_z \end{pmatrix}\nabla\rho\right)$$

where K_h, K_z are the horizontal and vertical Eddy diffusivities of density.

Consequently, the governing Navier–Stokes equations are,

$$\frac{\partial u}{\partial t} = -\frac{1}{\rho_0}\frac{\partial (p+q)}{\partial x} - (u,w)\cdot\nabla u + \nabla\cdot\left(\begin{pmatrix} A_h & 0 \\ 0 & Az \end{pmatrix}\nabla u\right), \tag{2.1}$$

$$\frac{\partial w}{\partial t} = -\frac{1}{\rho_0}\frac{\partial q}{\partial z} - (u,w)\cdot\nabla w + \nabla\cdot\left(\begin{pmatrix} A_h & 0 \\ 0 & A_z \end{pmatrix}\nabla w\right), \tag{2.2}$$

$$\frac{\partial \rho}{\partial t} = -(u,w)\cdot\nabla\rho + \nabla\cdot\left(\begin{pmatrix} K_h & 0 \\ 0 & K_z \end{pmatrix}\nabla\rho\right), \tag{2.3}$$

$$\nabla\cdot(u,w) = 0, \tag{2.4}$$

$$\frac{1}{\rho_0}\frac{\partial p}{\partial z} = \frac{-(\rho-\rho_0)g}{\rho_0}, \tag{2.5}$$

$$\frac{\partial q_s}{\partial t} = -\rho_0 g\frac{\partial}{\partial x}\int_{-h_0}^{\eta} u\mathrm{d}z. \tag{2.6}$$

To have a well-posed problem, initial and boundary conditions need to be prescribed. These are introduced in each example below.

Remark. In the application of interest, the variation of the free surface is much smaller than water depth. It can be neglected in the integral in the volume conservation equation. Consequently, our modification to the model in [8], is replacing the last equation by

$$\frac{\partial q_s}{\partial t} = -\rho_0 g\frac{\partial}{\partial x}\int_{-h_0}^{0} u\mathrm{d}z.$$

2.1. A Pressure Projection method

Pressure projection methods are well known, a thorough study is presented in [9].

Let us review the PP scheme for our application. Let Δt be the time step. Assume all variables are known at time t_n, $u^n, w^n, \rho^n, p^n, q^n$.

Let $q^{n+1} = q^n + \delta q^{n+1}$. The non-hydrostatic correction δq^{n+1} is to be determined. The main steps are:

Step 1. Update the density and the hydrostatic pressure

$$\frac{\rho^{n+1}-\rho^n}{\Delta t} = -(u^n,w^n)\cdot\nabla\rho^n + \nabla\cdot\left(\begin{pmatrix} K_h & 0 \\ 0 & K_z \end{pmatrix}\nabla\rho^n\right),$$

$$\frac{1}{\rho_0}\frac{\partial p^{n+1}}{\partial z} = \frac{-(\rho^n-\rho_0)g}{\rho_0},$$

Step 2. Construct intermediate velocities $u^{n+\frac{1}{2}}, w^{n+\frac{1}{2}}$ from

$$u^{n+\frac{1}{2}} = u^n - \frac{\Delta t}{\rho_0}\frac{\partial(p^{n+1}+q^n)}{\partial x} - \Delta t(u^n, w^n)\cdot\nabla u^n + \Delta t\nabla\cdot\left(\begin{pmatrix} A_h & 0 \\ 0 & Az\end{pmatrix}\nabla u^n\right),$$
$$w^{n+\frac{1}{2}} = w^n - \frac{\Delta t}{\rho_0}\frac{\partial q^n}{\partial z} - \Delta t(u^n, w^n)\cdot\nabla w^n + \Delta t\nabla\cdot\left(\begin{pmatrix} A_h & 0 \\ 0 & A_z\end{pmatrix}\nabla w^n\right).$$

Step 3. Compute the non-hydrostatic pressure correction by solving a Poisson equation

$$\frac{-\Delta t}{\rho}\Delta(\delta q^{n+1}) = -\nabla\cdot(u^{n+\frac{1}{2}}, w^{n+\frac{1}{2}}).$$

Step 4. Compute the divergence-free velocity field,

$$u^{n+1} = u^n - \frac{\Delta t}{\rho_0}\frac{\partial\delta q^{n+1}}{\partial x},$$
$$w^{n+1} = w^n - \frac{\Delta t}{\rho_0}\frac{\partial\delta q^{n+1}}{\partial z}.$$

Step 5. Update $q^{n+1} = q^n + \delta q^{n+1}$.

To discretize the advection terms in steps 1 and 2, we employ the well-known Total Variation Diminishing (TVD) scheme with the Superbee slope limiter, as described by [10]. Whereas, for the diffusion terms the basic central differences scheme is used.

Remark. Several days of simulation are required for the ocean modeling application of interest. To accelerate the computation, fast Poisson solvers are used in Step 3. Recently Discontinuous Galerkin (DG) and Hybrid Galerkin Methods (HDG) have been an attractive choice. This is because they are readily parallelizable. Literature on the subject is vast, we shall not be exhaustive and just mention the recent Discontinuous Galerkin method developed in [11] for elliptic equations. A drawback of DG methods is that they are generally more expensive than existing numerical methods because they have many more (coupled) unknowns. A recent solution is to introduce hybridizable (hybridized) Discontinuous Galerkin Methods (HDG). The number of coupled unknowns is reduced while retaining the attractive properties of the DG method, [12]. It is well known that these methods also require penalization for solving the underlying linear systems. This issue is still unresolved, see the discussion in Section D of [11], it is pointed out that there are penalty parameters to be prescribed. The choice is somewhat heuristic. For the Poisson problem, we have developed a simple non-penalized HDG method. A terse presentation is given in the Appendix.

2.2. A benchmark problem

As customary with Galerkin methods, for the Poisson solution, we use the classical Lagrange element basis functions on the reference segment $[-1,1]$ for 1D applications. We denote by HDG_p a p order bilinear approximation. In 2D, HDG_2, HDG_4 refer to basis functions on the reference square $[-1,1]\times[-1,1]$, as products of first-order, respectively second order 1D basis functions.

To report the approximation's accuracy, we use the Root Mean Square Error (RMSE). Here, we normalize by the corresponding norm of a reference solution to obtain the Normalized Root Mean Square Error (NRMSE).

We will test a benchmark problem in rectangular geometry and regular meshes for illustration. In [8] a closed channel is considered, it is initially composed of two vertical layers of water with constant but distinct density. The model is forced via the prescription of a layer of dense water that initially leans against the left boundary. The variable bottom topography includes a ramp and a vertical bar, see Figure 1.

The channel occupies the domain $\Omega = [0,500]\times[-100,0]$. The reference density is given by $\rho_0 = 1028\ \mathrm{kg\,m^{-3}}$, and a column of water with density $\rho_1 = 1029\ \mathrm{kg\,m^{-3}}$ is included in the region $\Omega^1 = [0,50]\times[-100,0]$.

The problem is solved in [8] with the classical second-order finite difference method (FD2).

The numerical solution is obtained using the grid spacing $\Delta x = 5m, \Delta z = 2m, \Delta t = 0.1s$. For the horizontal and vertical water diffusivities, we set $K_h = K_z = 10^{-4}\ \mathrm{m^2\,s^{-1}}$ and $A_h = A_z = 0$.

A comparison with the non-penalized HDG_2 method is presented in Figure 2. Relative errors with respect to the HDG_4 solution, carried out in the same grid, are shown in Table 1.

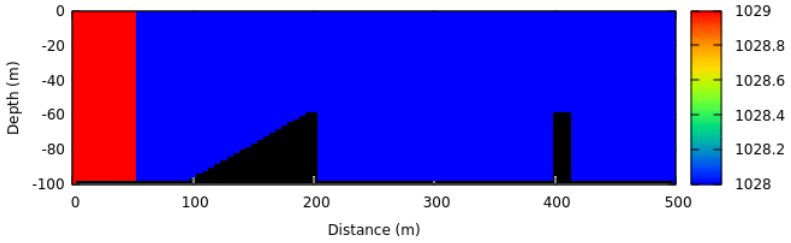

FIGURE 1. Initial density configuration and bathymetry.

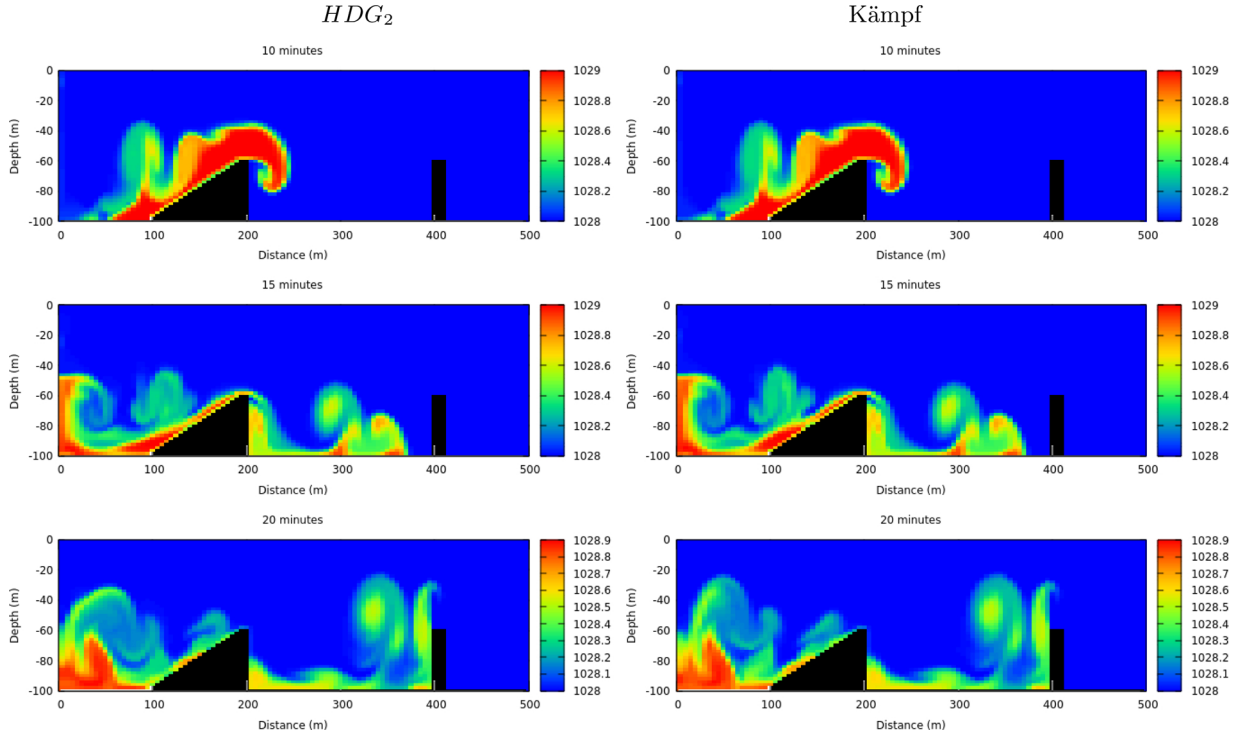

FIGURE 2. Density evolution for the variable bottom case using HDG_2 (left), and FD2 (right).

TABLE 1. Comparison of the HDG_2 and FD2 algorithms for the variable bottom case, taking the HDG_4 as a reference.

Time (min)	NRMSE(HDG_2)	NRMSE(Kämpf's)
7	6.55×10^{-5}	6.77×10^{-5}
9	0.00010759	0.000107866
13	0.000104016	0.000107906

Remark 2.1. We have tested exhaustively, and successfully, HDG_2 in most examples in [8]. Namely, Internal waves, Kelvin–Helmholtz instability, Lee waves, *etc.* The example presented here has been selected as preparation for the numerical modeling of the hydraulic jump in the next section.

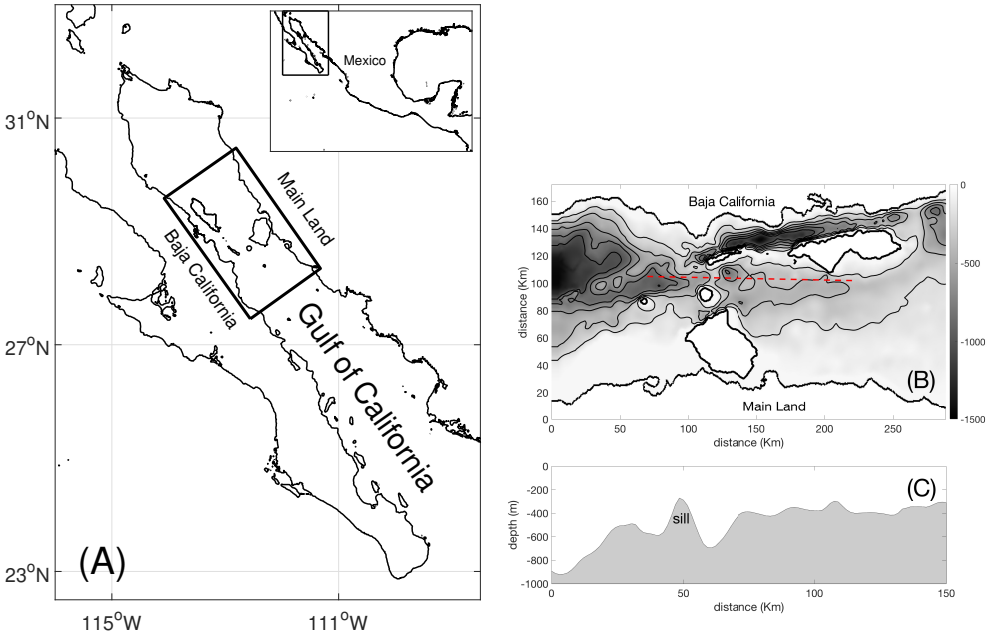

FIGURE 3. (A) Geographic location of the Gulf of California in Northwest Mexico. (B) The vertical section along the San Esteban Sill. (C) Numerical model domain.

3. The Gulf of California

The area of interest is a section between islands in the Gulf of California where the San Esteban sill is located, see Figure 3(A). The vertical slice under study in this work is along the dashed line, 3(C). The horizontal length of this section is 150 km, with a maximum depth of 900 m. The gray area in the background corresponds to the bathymetry, there is a seamount 50 km from the left, corresponding to the San Esteban Sill.

3.1. Initial and boundary conditions

The hydrographic characteristics of the Gulf of California (GC), such as stratification, internal tide, and bathymetric features, favor the generation and propagation of internal waves. The tide is one of the main forcings that control the dynamics of the GC, producing an inflow and outflow from the mouth of the Gulf to the northernmost part [3]. To derive the hydrodynamic model, these characteristics are introduced as initial and boundary conditions in the vertical slice Navier–Stokes equations.

3.1.1. Initial condition

The field velocities u, w and q, non-hydrostatic pressure, start at rest. The choice of the initial density profile requires some work. Considering the oceanographic conditions when data was collected, [5], we found, with a systematic exploration, that the depth variable density profile ($\rho(z)$) of October WOA2018 [13], is appropriate as an initial condition for density. The stratified density picture is in Figure 4.

3.1.2. The Poisson problem for the non-hydrostatic correction

The Poisson problem in Step 3 above, is solved in the domain in x between the inflow and outflow boundaries, say $[x_0, x_N]$, below the undisturbed surface water $z = 0$, and above the bathymetry h_0.

For later reference let $x_k = x_0 + k\Delta x$, $k = 1, 2, \ldots, N$ be the partition along the x axis. The boundary conditions for the non-hydrostatic correction δq^{n+1} are prescribed as follows.

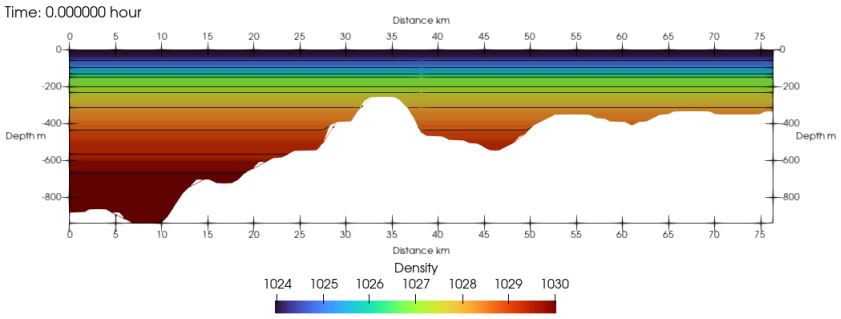

FIGURE 4. Vertical density distribution from October WOA2018.

Undisturbed surface water

Recall that

$$\frac{\partial q_s}{\partial t} = -\rho_0 g \frac{\partial}{\partial x} \int_{-h_0}^{0} u \mathrm{d}z.$$

Here, $g := 9.81 \frac{m}{s^2}$ and q_s the superficial non-hydrostatic pressure. An Euler discretization leads to

$$q_s^{n+1} - q_s^n = -\Delta t \rho_0 g \left(\frac{\partial}{\partial x} \int_{-h_0}^{0} u \mathrm{d}z \right) \Big|_{t=t_n}.$$

Consequently, at $z = 0$ the Dirichlet condition is

$$\delta q^{n+1} = -\Delta t \rho_0 g \left(\frac{\partial}{\partial x} \int_{-h_0}^{0} u \mathrm{d}z \right) \Big|_{t=t_n}.$$

Sea bottom boundary

At the bottom, we only consider impervious and rigid bathymetry. Thus a null Neumann condition is appropriate.

$$\nabla \delta q^{n+1} \cdot \mathbf{n} = 0$$

Since u, w start at rest, this condition in Step 4 implies zero normal velocity, that is, $(u^{n+1}, w^{n+1})^t \cdot \mathbf{n} = 0$.

Lateral boundaries

We assume no correction in the lateral boundaries, thus we prescribe the null Dirichlet conditions

$$\delta q^{n+1} \Big|_{x_0} = 0 = \delta q^{n+1} \Big|_{x_N}.$$

Implementation of boundary conditions in numerical methods is textbook material. In the HDG scheme, it is intrinsic to the numerical model.

3.2. Dynamic pressure boundary conditions

Notice that after the Poisson solution, all variables are updated in the interior. An extension to the lateral boundaries is accomplished by employing lateral boundary conditions for dynamic pressure and using the numerical scheme to predict boundary values of the velocities. It is well known that the latter provides consistency to the numerical scheme. See Section 5.13 in [8].

Inflow boundary

To model the forcing tide, a point located non-hydrostatic pressure sinusoidal variation is imposed with period T and amplitude A.

$$q^{n+1}(x_0, 0) = A \sin\left(\frac{2\pi t_{n+1}}{T}\right).$$

Because of the semidiurnal tide in the Gulf of California, we use a period $T = 12.4$hrs, and an amplitude $A = 0.5$m.

Outflow boundary

On the right boundary, a radiation condition is imposed to let the waves *go with the flow*, as influenced by the horizontal velocity. As pointed out above, this radiation condition should only be applied to dynamic pressure.

Since δq is zero at the outflow boundary, we consider the non-hydrostatic pressure q reaching such a boundary with speed c.

We solve locally the transport equation

$$\frac{\partial q}{\partial t} + c\frac{\partial q}{\partial x} = 0,$$

with an upwind scheme

$$q^{n+1}(x_N, z) = (1 - C)\, q^n(x_N, z) + C q^n(x_{N-1}, z),$$

where

$$C = |c|\frac{\Delta t}{\Delta x}.$$

For numerical stability $C \leq 1$.

The phase speed c, is approximated by

$$c = -\frac{\frac{\partial u^{n+1}(x_N, z)}{\partial t}}{\frac{\partial u^{n+1}(x_N, z)}{\partial x}} \approx -\frac{\Delta x}{\Delta t}\frac{u^{n+1}(x_{N-1}, z) - u^n(x_{N-1}, z)}{u^{n+1}(x_{N-1}, z) - u^{n+1}(x_{N-2}, z)}.$$

3.3. Numerical model configuration

In the Boussinesq approximation, one usually assumes that the density varies linearly with temperature. In the problem of concern, no substantial temperature gradients occur, and it is sufficient to approximate the horizontal and vertical Eddy viscosities, A_h, A_z, by constants. Similarly the vertical Eddy diffusivities of density K_h, K_z.

In the simulation we use

$$A_h = A_z = 10^{-7}\,\mathrm{m^2\,s^{-1}}, \quad K_h = K_z = 10^{-4}\,\mathrm{m^2\,s^{-1}}.$$

For the semidiurnal tide that occurs in the Gulf of California a period $T = 12.4$ h is used. The working amplitude is $A = 0.5$ m.

The model was running for ten days with data output every 2 min. We show results for the grid with $\Delta x = 100\,\mathrm{m}$, $\Delta z = 20\,\mathrm{m}$, and $\Delta t = 0.1\,\mathrm{s}$.

We zoom in on the region around the San Esteban Sill.

3.4. The hydraulic jump

The numerical model results are shown in vertical slices, that is, a plane where the horizontal axis is the distance along the Gulf and the vertical axis is depth.

To describe the dynamics of the internal tide passing through the San Esteban Sill, Figure 5 shows the lines of equal density (isopycnal), and the black arrows, are the flow velocity (vertical component was multiplied by 5 to appreciate it). In the initial state, the isopycnals are horizontal and as forcing is applied at the left end of the domain, a current is produced that enters and leaves the domain on the right side, causing the isopycnals to shift. When the level of the surface rises on the left side, a current is produced to the right and when trying to pass over the San Esteban Sill, an increase in speed is produced to maintain the flow. On the Sill and towards the right side a flow of greater speed is formed attached to the bottom, producing the hydraulic jump (Fig. 5 upper). During the development of the hydraulic jump, the increase in bottom velocity causes the isopycnals to bend downwards on the Sill, generating a sudden change in density and strong mixing (Fig. 5 lower).

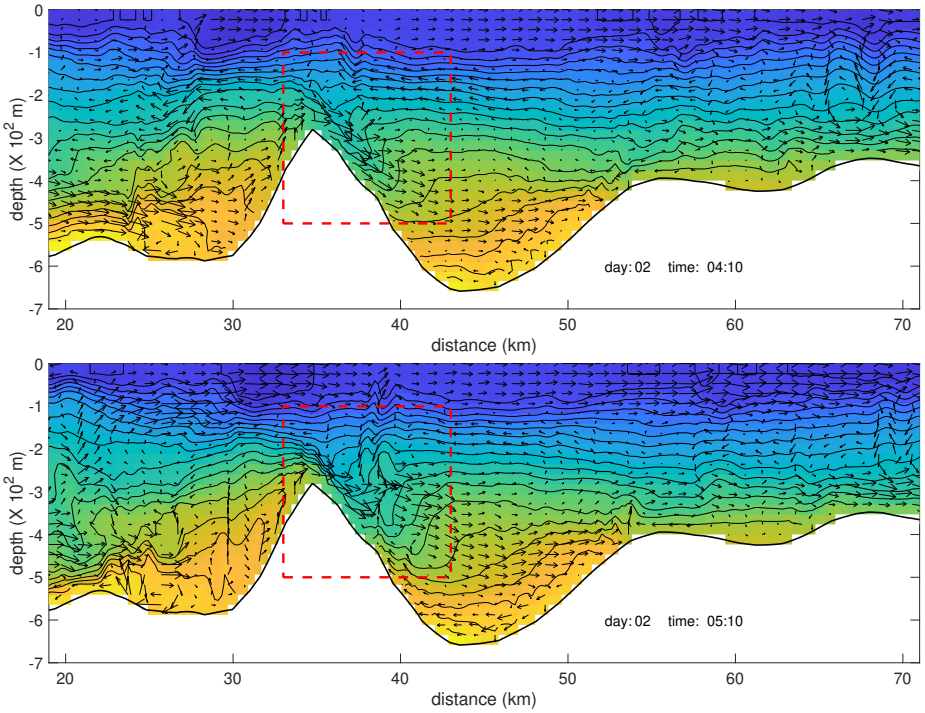

FIGURE 5. Density (color and contours) and velocity (arrows) for (upper) hydraulic jump produced by tidal forcing and (lower) strong mixing that can be observed inside the rectangle dashed red line.

As the current flow is still to the right when the isopycnals are deformed, this disturbance is pushed by the current to the right, giving rise to an internal wave packet (Fig. 5b). In this case, the temporal sequence of images of the isopycnals during the entry flow (flow to the right) allows us to observe that when the flow passes over the Sill it increases its speed, causing convergence with the flow that is to the right of the Sill, that moves with less speed causing the deformation of the isopycnals similar to an accordion folds.

3.5. Internal waves

After reviewing the data from the numerical model, we find that the speed at which the internal wave packets propagate is on average 0.66 $\mathrm{m\,s^{-1}}$, with an amplitude of 47 meters and a distance between crests of 1.5 km. Figure 6 shows one slice of the numerical model vertical velocity at the time (hh:mm) 14:30 for the second day of simulation where colors refer to the vertical velocity component and the black lines, are the density contours. We show in these slices, that the isopycnal deformation is accompanied by a variation of the vertical velocity in positive and negative bands as was reported by [5] and that corresponds to a wave packet released from the sill after the passage of an internal tidal wave.

Taking the time series of model outputs variables at all depth levels, at 55 km horizontal distance, we show in Figure 7 two time-depth slices to see the passage of the internal wave packets for both velocity components Figure 7a horizontal and Figure 7b vertical and the density variation as black contours. In these Figures 7 the black dashed rectangles show the two most intense events during the second day of simulation.

4. Discussion and conclusions

The configuration of the model used for the San Esteban Sill region, forced by the tidal variation, generates a hydraulic jump over the Sill upstream when the flow is towards the interior of the Gulf (to the right in our domain). When the flow slows down, it generates a packet of internal waves. Based on the internal wave observations by [5], these internal wave packets can be observed in velocity components and density. In our case, the model generates as outputs variables

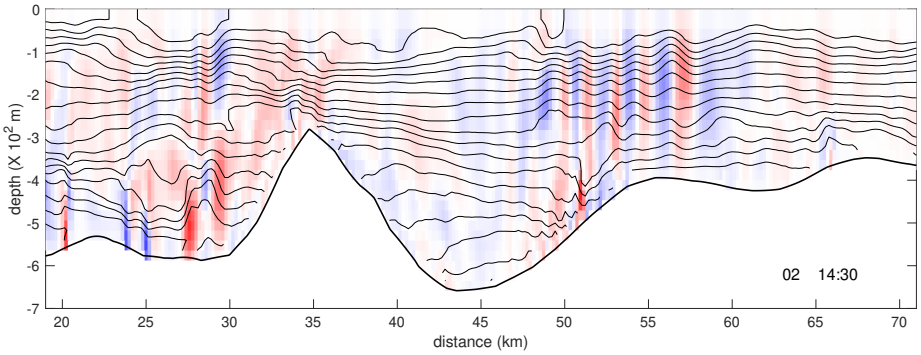

FIGURE 6. Slice of vertical velocity component (color tones) and density contours showing the snapshot of internal wave travel to the right after the sill.

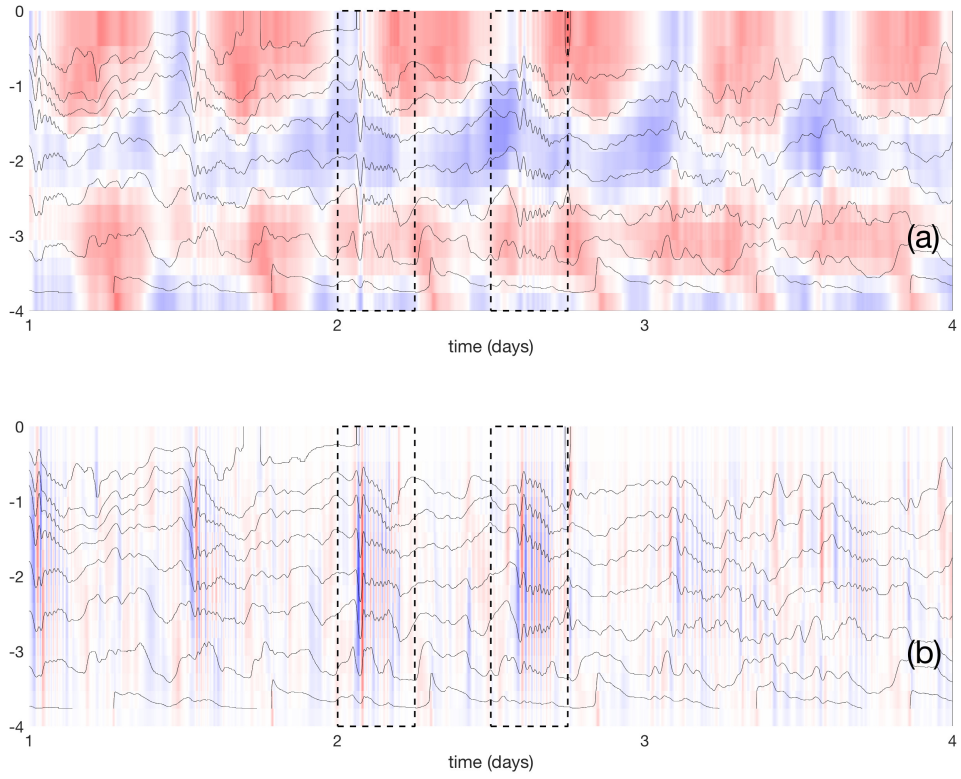

FIGURE 7. time series profile at a distance of 55 km in the model domain for (a) horizontal and (b) vertical velocity components (black contours correspond to density). Dashed rectangles show the passage of internal wave packets.

density fields and two velocity components, one horizontal along the slice and the other vertical. In these three physical variables, we were able to observe the signature of the internal wave packet. To identify the presence of the hydraulic jump above the San Esteban Sill, we calculate the Froude Number (Fr) along the x-axis and find that the highest values occur just to the right of the Sill. Once the Hydraulic Jump is formed, we can corroborate that a package of internal waves is released to the right of the Gulf, with the same characteristics described by [5].

The implementation of the Pressure Projection method, with non penalized HDG Poisson solver, shows to be an efficient way to solve the non-hydrostatic Navier–Stokes equations for ocean circulation. This methodology allows us to solve a large number of nodes in a short computational time to simulate with sufficient resolution the phenomenon of internal waves, thus fulfilling our modeling focus. An in-depth work on the numerical aspects and comparison with other methods is part of ongoing research. It shall be reported elsewhere.

Of current and future interest, is to extend the model to 3D and other field cases. A theory confirming that the generation of internal waves is due to the hydraulic jump is left for future investigations.

Appendix: A

The Poisson Solver

This terse presentation follows [12]. Let Ω be a bounded Lipschitz domain in $\mathbb{R}^2$. Consider the Poisson equation

$$-\Delta q = b.$$

Let us define the new variable (the flux) $\mathbf{z} = -\nabla q$. We are led to the first order system

$$\begin{aligned} \nabla q + \mathbf{z} &= 0, \\ \nabla \cdot \mathbf{z} &= b. \end{aligned}$$

Now consider the matrices,

$$\mathbf{u} := (\mathbf{z}, q)^T, \mathbf{b} := (0, b)^T, \mathcal{A}_1 := \begin{pmatrix} 0 & 0 & 1 \\ 0 & 0 & 0 \\ 1 & 0 & 0 \end{pmatrix}, \mathcal{A}_2 := \begin{pmatrix} 0 & 0 & 0 \\ 0 & 0 & 1 \\ 0 & 1 & 0 \end{pmatrix}, \mathcal{B} := \begin{pmatrix} 1 & 0 & 0 \\ 0 & 1 & 0 \\ 0 & 0 & 0 \end{pmatrix}.$$

The previous system of equations is written in the compact form

$$\nabla \cdot (\mathcal{A}_1 \mathbf{u}, \mathcal{A}_2 \mathbf{u}) + \mathcal{B}\mathbf{u} = \mathbf{b}.$$

Let us define the flux function $\mathcal{F}(\mathbf{u}) := (\mathcal{A}_1 \mathbf{u}, \mathcal{A}_2 \mathbf{u})$, the system becomes

$$\nabla \cdot \mathcal{F}(\mathbf{u}) + \mathcal{B}\mathbf{u} = \mathbf{b}. \tag{A.1}$$

Assume we have a valid element partition of the domain Ω. In DG, functions are approximated locally in each element by polynomials, then coupled with others in adjacent elements by means of a numerical flux. The basic process is as follows. Let τ be an element in the partition. Compute the $(L^2)^3$ inner product on τ of each side of (A.1) with a (polynomial) test function $\mathbf{v}$, to obtain

$$(\nabla \cdot \mathcal{F}(\mathbf{u}), \mathbf{v})_\tau + (\mathcal{B}\mathbf{u}, \mathbf{v})_\tau = (\mathbf{b}, \mathbf{v})_\tau. \tag{A.2}$$

Integrating by parts,

$$-(\mathcal{F}(\mathbf{u}), \nabla \mathbf{v})_\tau + \langle \mathcal{F}(\mathbf{u}) \cdot \mathbf{n}, \mathbf{v} \rangle_{\partial\tau} + (\mathcal{B}\mathbf{u}, \mathbf{v})_\tau = (\mathbf{b}, \mathbf{v})_\tau, \tag{A.3}$$

Continuity is not enforced at the boundary of adjacent elements. Therefore, the boundary term $\mathcal{F}(\mathbf{u})$ is replaced with a boundary numerical flux $\mathcal{F}^*(\mathbf{u}^*)$ where $\mathbf{u}^* \equiv \mathbf{u}^*(\mathbf{u}^-, \mathbf{u}^+)$ solves a Riemann problem with Cauchy data $\mathbf{u}^-$, $\mathbf{u}^+$. As customary, the $-$ superscript denotes limits from the interior of F, and the $+$ superscript, limits from the exterior. In this context, element τ is denoted by τ^- and the outer normal $\mathbf{n}$ by $\mathbf{n}^-$. To hybridize the flux, and break the coupling, $\mathbf{u}^*$ is regarded as an extra unknown to be solved on the skeleton of the mesh, that is the set of sides (edges) of elements. Renaming $\mathbf{u}^*$ as $\hat{\mathbf{u}}$ and $\mathcal{F}^*$ as $\hat{\mathcal{F}}$, the problem is to propose a suitable hybrid numerical flux $\hat{\mathcal{F}}(\mathbf{u})$. Instead of the Riemann problem solution approach, we propose the hybrid flux

$$\hat{\mathcal{F}} \cdot \mathbf{n} = \begin{pmatrix} \hat{q}\mathbf{n} \\ \mathbf{z} \cdot \mathbf{n} + q - \hat{q} \end{pmatrix}. \tag{A.4}$$

Notice dependence only in the unknown $\hat{q}$. For each element τ, the DG local unknown $\mathbf{u}$ and the extra *trace* unknown $\hat{q}$ need to satisfy

$$-(\mathcal{F}(\mathbf{u}), \nabla \mathbf{v})_\tau + \langle \hat{\mathcal{F}} \cdot \mathbf{n}, \mathbf{v} \rangle_{\partial\tau} + (\mathcal{B}\mathbf{u}, \mathbf{v})_\tau = (\mathbf{b}, \mathbf{v})_\tau, \tag{A.5}$$

This is complemented by a weak jump condition in the skeleton. Namely, for each edge F

$$(\llbracket \mathbf{z} \cdot \mathbf{n} + q - \hat{q} \rrbracket, w)_F = 0. \tag{A.6}$$

Where $\mathbf{v}$ in (A.5), w in (A.6) are polynomial test functions defined on elements τ and edges F respectively. Here, $[\![\cdot]\!]$ is the jump operator,

$$[\![(\cdot)]\!] = (\cdot)^- + (\cdot)^+.$$

On each element, we are led to solve the equations (A.5) and (A.6).

Let us split the test function in the form $\mathbf{v} = (\mathbf{w}, w)$. The equation (A.5) using the hybrid flux can be written as

$$-(q, \nabla \cdot \mathbf{w})_\tau + (\hat{q}, \mathbf{w} \cdot \mathbf{n})_{\partial\tau} + (\mathbf{z}, \mathbf{w})_\tau = 0, \tag{A.7}$$

$$-(\mathbf{z}, \nabla w)_\tau + (\mathbf{z} \cdot \mathbf{n} + q - \hat{q}, w)_{\partial\tau} = (b, w)_\tau. \tag{A.8}$$

Let us show that this finite-dimensional problem is well-posed by showing that under null data, the solution is the trivial one.

Lemma A.1. *If $b(x) = 0$ and $\hat{q} = 0$ on $\mathfrak{F}$, then $q = 0, \mathbf{z} = \mathbf{0}$ in Ω.*

Proof. By integration by parts in (A.8)

$$(\nabla \cdot \mathbf{z}, w)_\tau + (q, w)_{\partial\tau} = 0. \tag{A.9}$$

Let $\mathbf{w} = \mathbf{z}, w = q$, and add equations (A.7), (A.9) to obtain

$$(\mathbf{z}, \mathbf{z})_\tau + (q, q)_{\partial\tau} = 0.$$

Hence, $q^- = 0$ on $\partial\tau$, and $\mathbf{z} = \mathbf{0}$ in τ. Equation (A.7) becomes

$$-(q, \nabla \cdot \mathbf{w})_\tau = 0.$$

Integrating by parts

$$-(q^-, \mathbf{w} \cdot \mathbf{n})_{\partial\tau} + (\nabla q, \mathbf{w})_\tau = 0.$$

$$(\nabla q, \mathbf{w})_I = 0.$$

Since $\mathbf{w}$ is arbitrary, $\nabla q = 0$, and consequently $q \equiv 0$ in each element.

We conclude that $q = 0, \mathbf{z} = \mathbf{0}$ in Ω. □

Remark. A conclusion of this result, is that to solve the equations (A.5) and (A.6), there is no need for penalization for the Poisson problem, unlike the classical application of DG methods for elliptic equations, [11].

Acknowledgements

We want to thank the referees for their very constructive comments, which have improved the manuscript.

References

[1] J.C Garwood, R.C. Musgrave and A.J. Lucas, Life in internal waves. *Oceanography* **33** (2020) 38–49.

[2] R.N. Ibragimov and A. Tartakovsky, Spectral analysis of the efficiency of vertical mixing in the deep ocean due to interaction of tidal currents with a ridge running down a continental slope. *Math. Model. Natural Phenomena* **9** (2014) 119–137.

[3] M.F. Lavín and S.G. Marinone, An overview of the physical oceanography of the gulf of california. *Nonlinear Processes in Geophysical Fluid Dynamics: a tribute to the scientific work of Pedro Ripa* (2003) 173–204.

[4] F.A. Velazquez-Muñoz and A. Filonov, Tidal energy flows between the midriff islands in the gulf of California. *Energies* **14** (2021) 621.

[5] A. Filonov, I. Tereshchenko, L.B. Ladah, D.A. Pantoja-Gonzalez and F.A. Velázquez-Muñoz, High amplitude internal tidal waves generated over an underwater sill in the gulf of california. *Continent. Shelf Res.* **210** (2020) 104290.

[6] A.F Blumberg and G.L. Mellor, A description of a three-dimensional coastal ocean circulation model. *Three-dimensional Coastal Ocean Models* **4** (1987) 1–16.

[7] C. Ai, Y. Ma, C. Yuan and G. Dong, Non-hydrostatic model for internal wave generations and propagations using immersed boundary method. *Ocean Eng.* **225** (2021) 108801.

[8] J. Kämpf, Advanced Ocean Modelling: Using Open-source Software. Springer Science & Business Media (2010).

[9] A.S. Almgren, J.B. Bell and W.Y. Crutchfield, Approximate projection methods: Part I. Inviscid analysis. *SIAM J. Sci. Comput.* **22** (2000) 1139–1159.

[10] O.B. Fringer, S.W. Armfield and R.L. Street, Reducing numerical diffusion in interfacial gravity wave simulations. *Int. J. Numer. Methods Fluids* **49** (2005) 301–329.

[11] N.L Fischer and H.P. Pfeiffer, Unified discontinuous Galerkin scheme for a large class of elliptic equations. *Phys. Rev. D* **105** (2022) 024034.

[12] T. Bui-Thanh, From Godunov to a unified hybridized discontinuous Galerkin framework for partial differential equations. *J. Computat. Phys.* **295** (2015) 114–146.

[13] R.A. Locarnini, T.P. Boyer, A.V. Mishonov, J.R. Reagan, M.M. Zweng, O.K. Baranova, H.E. Garcia, D. Seidov, K.W. Weathers, C.R. Paver *et al.*, World Ocean Atlas 2018, Vol. 5: Density. *NOAA Atlas NESDIS* **85** (2019) 41.